

Directional Dark Matter Detection in Anisotropic Dirac Materials

Ahmet Coskuner,^{1,2} Andrea Mitridate,^{3,4} Andres Olivares,⁵ and Kathryn M. Zurek⁶

¹*Berkeley Center for Theoretical Physics,*

University of California, Berkeley, CA 94720, USA

²*Department of Physics, University of California, Berkeley, CA 94720, USA*

³*Scuola Normale Superiore, Piazza dei Cavalieri 7, 56126, Pisa, Italy*

⁴*INFN sezione di Pisa, Italy*

⁵*Institute for Particle Physics Phenomenology,*

Department of Physics, Durham University,

South Road, Durham DH1 3LE, United Kingdom

⁶*Walter Burke Institute for Theoretical Physics,*

California Institute of Technology, Pasadena, CA 91125

Abstract

Dirac materials, because of unique symmetries near the Fermi surface, are a promising target for dark photon-mediated scattering and absorption of light dark matter. In this paper, we characterize the daily modulation rate of dark matter interacting with a Dirac material due to anisotropies in the crystal structure of typical Dirac materials, and we show that daily modulation is $\mathcal{O}(1)$ of the total rate for the Dirac material ZrTe₅. These modulation effects depend on the orientation of the material’s Fermi velocity and permittivity tensor with respect to the dark matter wind, and they are maximized when the crystal is oriented such that the dark matter wind is completely aligned with the largest and smallest components of the Fermi velocity at two different times of the day. Because of the large modulation, any putative dark matter signal could be rapidly verified or ruled out by changing the orientation of the crystal with respect to the wind and observing how the daily modulation pattern changes.

CONTENTS

I	Introduction	2
II	Dark Matter Interactions with In-Medium Effects	4
A	Optical properties of anisotropic Dirac Materials	6
III	Preliminaries: Dark Matter Wind	7
IV	Absorption in Anisotropic Dirac Materials	9
V	Scattering in Anisotropic Dirac Materials	12
A	Origin of the daily modulation	15
VI	Conclusions	19
A	In medium polarization tensor	20
	References	21

I. INTRODUCTION

The direct detection of dark matter has seen a dramatic broadening of scope beyond the traditional domains of the search for the Weakly Interacting Massive Particle (WIMP) and the axion. Both are highly motivated by solving other problems in the SM sector, such as the hierarchy problem (WIMP) and the strong CP problem (axion). However, the WIMP has been increasingly constrained by highly sensitive experiments that have searched for new physics at the weak scale for decades.

At the same time, visible and dark matter may originate from two separate sectors, independent of any problems in the SM [1]. The development of the hidden sector paradigm has opened a fruitful direction in building models of dark matter. Similar to the SM, the lightest particle of the dark sector may be stable thanks to a gauge or global symmetry. The interactions with the SM may be only gravitational, or mediated by new forces that interact only very feebly with the dark and/or visible sectors. However, these feeble interactions with the SM may be crucial in setting the dark matter abundance, as is typical, for example, in models of MeV dark matter [2–4], WIMPless miracle DM [5], Asymmetric DM [6, 7], GeV hidden sector dark matter [8–10], freeze-in DM [11], and Strongly Interacting Massive Particles [12]. In this case, well-motivated and clear benchmarks exist to search for dark matter in hidden sectors. Two classic examples

are Asymmetric Dark Matter annihilating its symmetric abundance through the dark photon [13], as well as dark-photon mediated dark matter produced through a freeze-in process [14, 15].

While there are many well-motivated models, if the mass of the dark matter in the hidden sector is below approximately a GeV, existing technologies to search for the WIMP through nuclear recoils are not sensitive to it. However, recent years have seen the development of many new ideas to detect sub-GeV dark matter (see Ref. [16] for an extensive review). When the dark matter carries more energy than electronic excitation energies—typically in the 1-10 eV range, corresponding to the kinetic energy of 1-10 MeV dark matter–semiconductor [17–19] or noble liquid [20] targets developed to search for the WIMP through nuclear recoils with keV energy deposition can be extended to search instead for valence-to-conduction-band transitions or ionization. The challenge is to reduce dark counts and increase sensitivity to energy depositions three orders of magnitude below that needed for WIMPs. This program is well under way in noble liquid [21] and silicon targets, and is actively being pursued in collaborations such as SENSEI [22–24], DAMIC [25, 26] and SuperCDMS [27–31].

When the DM mass drops below an MeV, new ideas and targets must be found. This has been the focus of intense efforts on small gap materials, such as superconductors [32, 33], graphene [34], and Dirac Materials [35] in the case of electronic excitations, and superfluid helium [36, 37] and polar materials [38] when the DM couples to nuclei or ions. In this paper, we will focus on electronic excitations, and in particular dark photon mediated couplings to electrons.

If the dark matter interaction with the SM arises through a dark photon kinetically mixed with the visible photon, in-medium effects on the kinetic mixing between the dark and visible photons have been shown to have a dramatic effect [33]. In particular, the effective coupling (as we review below) between the dark photon and the electromagnetic current is given by

$$\mathcal{L} = \epsilon e \frac{q^2}{q^2 - \Pi_{T,L}} \tilde{A}'_\mu^{T,L} J_{EM}^\mu, \quad (1)$$

where $\Pi_{T,L}$ are the in-medium polarization tensor of the visible photon, which we will define precisely below. In an optically responsive material like superconductors, its value is set by the Thomas-Fermi screening length, $\lambda_{TF}^2 = 3e^2 n_e / (2E_F)$, which is on the order of 10 keV. Since the maximum momentum transfer is $q_{\max} = 2m_\chi v_\chi$, for sub-MeV DM, the in-medium suppression due to the polarization tensor is substantial. This is because there is no symmetry to protect the photon from gaining a large in-medium “mass.”

Dirac materials were proposed in Ref. [35] as an antidote to this problem. Dirac materials are so named because near the Fermi level, the electron dispersion obeys the Dirac equation for a relativistic free electron. This also means that these electrons have the same gauge symmetries as quantum electrodynamics. In QED, the photon is protected from obtaining a mass due

to the $U(1)_{EM}$ gauge symmetry¹; instead of obtaining a mass through quantum corrections, the charge is renormalized. By virtue of satisfying the Dirac equation, precisely the same phenomenon occurs in Dirac materials: the photon does not receive a (momentum-independent) in-medium mass. Instead, $\Pi_{T,L}$ receives a contribution proportional to \mathbf{q}^2 analogous to charge renormalization. Thus Dirac materials have a strong coupling to kinetically mixed dark photons, and an excellent reach to dark matter mediated through this interaction.

The goal of this paper is to explore in detail an important property of Dirac materials that has implications for direct detection, their anisotropy: both the electron Fermi velocities, which dominate the kinematics of the DM-electron scattering, and the permittivity tensor, which characterizes the strength of the electron interactions with the dark photon, are highly dependent on the crystal axis. This implies that the dark matter interaction rate should depend on the orientation of the crystal with respect to the dark matter wind inducing a daily modulation of the interaction rate. While this feature was observed in Ref. [35], we calculate this effect here. We find that these modulation effects are of $\mathcal{O}(1)$; and that, since the modulation turns out to be dominated by anisotropies in the crystal band structure, they can be maximized orienting the crystal in such a way that the DM wind is completely aligned with the smallest and largest component of the Fermi velocity at two different times of the day. Strong anisotropy and daily modulation in sub-MeV dark matter interaction rates are also a feature of polar materials, as proposed in Ref. [39], though in Dirac Materials the interaction is with electrons rather than ions. Other proposals for directional detection of DM candidates include using two-dimensional materials like graphene [34] in the case of DM coupling to electrons; defect production in crystals [40, 41], and nuclear recoils in semiconductors [42].

The outline of this paper is as follows. In the next Section we lay out the formalism for calculating dark matter interactions with in-medium effects. In Sec. III, we define our conventions for the orientation of the crystal with respect to the DM wind. Then in Secs. IV and V, we compute the anisotropic absorption and scattering rates. Finally we conclude.

II. DARK MATTER INTERACTIONS WITH IN-MEDIUM EFFECTS

As explained in the introduction, Dirac materials are most powerful in setting strong constraints relative to other materials when the DM interaction occurs via the electromagnetic current. Specifically, we consider a kinetically mixed dark photon,

$$\mathcal{L} \supset -\frac{1}{4}F_{\mu\nu}F^{\mu\nu} - \frac{1}{4}F'_{\mu\nu}F'^{\mu\nu} - \frac{\varepsilon}{2}F_{\mu\nu}F'^{\mu\nu} + eJ_{EM}^\mu A_\mu + g_D J_{DM}^\mu A'_\mu + \frac{m_{A'}^2}{2}A'^\mu A'_\mu, \quad (2)$$

¹ We thank Yoni Kahn for pointing out that this is a feature of any semiconductor with a valence-to-conduction transition (satisfying the Lindhard formula) where the conduction band is unoccupied.

where $F_{\mu\nu}$ ($F'_{\mu\nu}$) is the electromagnetic (dark) field strength, ε the kinetic mixing parameter and $J_{\text{EM (DM)}}^\mu$ the electromagnetic (dark) current that couples to (dark) photons with a coupling e (g_D). The dark photon has a mass $m_{A'}$ which can be generated either by a dark Higgs or through the Stueckelberg mechanism (though astrophysical constraints are weakest for the case of a Stueckelberg dark photon). In the vacuum, the propagating photon (found by diagonalizing the kinetic term in Eq. (2)) is $\tilde{A}_\mu = A_\mu - \varepsilon A'_\mu$. In this basis the dark photon mass eigenstate A' couples to the electromagnetic current with a strength $e\varepsilon$.

Because of this coupling, the propagation of a dark photon in optically responsive media is modified. Specifically, including in-medium effects, the Lagrangian Eq. (2) (using the \tilde{A} , A' basis) takes the form

$$\mathcal{L} \supset -\frac{1}{4}\tilde{F}_{\mu\nu}\tilde{F}^{\mu\nu} - \frac{1}{4}F'_{\mu\nu}F'^{\mu\nu} + eJ_{\text{EM}}^\mu(\tilde{A}_\mu + \varepsilon A'_\mu) + g_D J_{\text{DM}}^\mu A'_\mu + \frac{m_{A'}^2}{2}A'^\mu A'_\mu \quad (3)$$

$$-\frac{1}{2}\tilde{A}^\mu\Pi_{\mu\nu}\tilde{A}^\nu - \varepsilon\tilde{A}^\mu\Pi_{\mu\nu}A'^\nu \quad (4)$$

where the in-medium polarization tensor is defined as $\Pi_{\mu\nu} \equiv ie^2\langle J_{\text{EM}}^\mu J_{\text{EM}}^\nu \rangle$, and the equation of motion has been used to derive the last line. In the familiar case of isotropic materials, the polarization tensor can be written as $\Pi^{\mu\nu} = \Pi_T(\epsilon_+^\mu\epsilon_+^\nu + \epsilon_-^\mu\epsilon_-^\nu) + \Pi_L\epsilon_L^\mu\epsilon_L^\nu$, with ϵ_L and $\epsilon_{+,-}$ the longitudinal and transverse polarization vectors. For $q \parallel \hat{z}$, they can be written as:

$$\epsilon_L = \frac{1}{\sqrt{q^2}}(|\mathbf{q}|, \omega \hat{q}) \quad \epsilon_{\pm} = \frac{1}{\sqrt{2}}(0, 1, \pm i, 0). \quad (5)$$

One then finds that transverse and longitudinal dark photons remain decoupled during their propagation in the medium and interact with the electromagnetic current with reduced couplings [33]:

$$\mathcal{L} \supset \varepsilon e \frac{q^2}{q^2 - \Pi_{L,T}} A'^{T,L}_\mu J_{\text{EM}}^\mu. \quad (6)$$

In the case of anisotropic materials, the polarization tensor cannot be decomposed into a longitudinal and a transverse component. This induces a mixing between longitudinal and transverse polarizations that can be parametrized in terms of a symmetric 3×3 mixing matrix, \mathcal{K} , defined as

$$\mathcal{K}_{AB} \equiv \epsilon_A^\mu \Pi_{\mu\nu} \epsilon_B^\nu, \quad (7)$$

with A and B running over longitudinal and transverse polarizations. It is therefore useful to choose a basis, $\tilde{\epsilon}_i$, for the physical polarizations that is not mixed by in-medium propagation. This basis is found using the 3×3 unitary matrix, \mathcal{S} , that diagonalizes the mixing matrix:

$$(\tilde{\epsilon}_1^\mu, \tilde{\epsilon}_2^\mu, \tilde{\epsilon}_3^\mu) = \mathcal{S} \begin{pmatrix} \epsilon_L^\mu \\ \epsilon_+^\mu \\ \epsilon_-^\mu \end{pmatrix} \quad \text{with} \quad \mathcal{S}^{-1}\mathcal{K}\mathcal{S} = \text{diag}(\pi_1(q), \pi_2(q), \pi_3(q)). \quad (8)$$

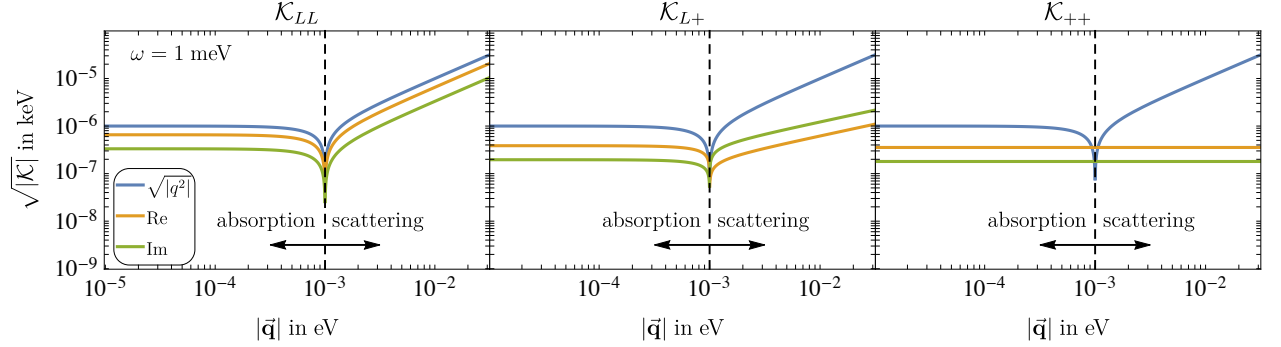


FIG. 1. The (square root of the) imaginary and real parts of the mixing matrix components as a function of the momentum transfer $|\vec{q}|$, in order to demarcate the absorption ($\mathbf{q}^2 \ll \omega^2$) and the scattering ($\mathbf{q}^2 \gg \omega^2$) regime indicated by the vertical dashed line. To obtain the plot we consider an energy deposition of $\omega = 1 \text{ meV}$, and an arbitrary orientation $\hat{q} = \frac{1}{\sqrt{3}}(1, 1, 1)$.

In this new basis, the Lagrangian of Eq. (3) takes the form

$$\mathcal{L} \supset -\frac{1}{4}\tilde{F}_{\mu\nu}^i\tilde{F}_i^{\mu\nu} - \frac{1}{4}F_{\mu\nu}^{i'}F_i'^{\mu\nu} + eJ_{\text{EM}}^\mu \left(\tilde{A}_\mu^i + \varepsilon A_\mu^{i'} \right) + g_D J_{\text{DM}}^\mu A_\mu^{i'} + \frac{m_{A'}^2}{2} A_i'^\mu A_\mu^{i'} \quad (9)$$

$$+ \frac{\pi_i}{2} \tilde{A}_\mu^i \tilde{A}_i^\mu + \varepsilon \pi_i \tilde{A}_\mu^i A_i'^\mu \quad (10)$$

and can be diagonalized making the following field redefinition:

$$\bar{A}_\mu^i = \tilde{A}_\mu^i + \frac{\varepsilon \pi_i(q)}{m_{A'}^2 - \pi_i(q)} A_\mu^{i'} \quad \bar{A}_\mu^{i'} = A_\mu^{i'} + \frac{\varepsilon \pi_i(q)}{m_{A'}^2 - \pi_i(q)} \tilde{A}_\mu^i. \quad (11)$$

One then finds that the propagating dark photons \bar{A}_i' couple to the electromagnetic current as:

$$\mathcal{L} \supset \varepsilon e \frac{q^2}{q^2 - \pi_i} \bar{A}_\mu^{i'} J_{\text{EM}}^\mu. \quad (12)$$

Thus we see that in the anisotropic case the role of $\Pi_{L,T}$ is played by the mixing matrix eigenvalues π_i .

A. Optical properties of anisotropic Dirac Materials

Working in Lorentz gauge, the in-medium photon propagator takes the form

$$G_{\text{med}}^{\mu\nu}(q) = \sum_i \frac{P_i^{\mu\nu}}{\pi_i - q^2} \quad (13)$$

where $q = (\omega, \mathbf{q})$ is the four-momentum transfer and P_i is the projector operator on the direction of the i -th polarization. In order to compute the eigenvalues of the mixing matrix, we relate its components to the optical properties of the medium (see appendix A for details):

$$\mathcal{K}_{LL} = q^2 (1 - \hat{\mathbf{q}} \cdot \boldsymbol{\epsilon} \cdot \hat{\mathbf{q}}) \quad \mathcal{K}_{L\pm} = -\omega q \hat{\mathbf{q}} \cdot \boldsymbol{\epsilon} \cdot \hat{\epsilon}_\pm \quad \mathcal{K}_{\pm\pm} = \omega^2 (1 - \hat{\epsilon}_\pm \cdot \boldsymbol{\epsilon} \cdot \hat{\epsilon}_\pm) \quad (14)$$

where $\boldsymbol{\epsilon}$ is the permittivity tensor which, for gapless materials, takes the form [35]:

$$\boldsymbol{\epsilon}(\mathbf{q}) = \mathcal{I} - \frac{\boldsymbol{\kappa}^{-1}}{\mathbf{q}^2} \frac{e^2 g}{24\pi^2 v_{F,x} v_{F,y} v_{F,z}} \left\{ -\tilde{\mathbf{q}}^2 \ln \left| \frac{4\tilde{\Lambda}^2}{\omega^2 - \tilde{\mathbf{q}}^2} \right| - i\pi \tilde{\mathbf{q}}^2 \Theta(\omega - |\tilde{\mathbf{q}}|) \right\} \quad (15)$$

where $\boldsymbol{\kappa} = \text{Diag}(\kappa_{xx}, \kappa_{yy}, \kappa_{zz})$ is the background dielectric tensor, $\tilde{\mathbf{q}} = (v_{F,x} q_x, v_{F,y} q_y, v_{F,z} q_z)$, $\tilde{\Lambda} = \Lambda \times \max(v_{F,x}, v_{F,y}, v_{F,z})$ and $g = g_s g_C$ is the product of spin and Dirac cone degeneracy. Theoretical values of the dielectric tensor components and Fermi velocities for ZrTe₅ are reported in Table I. For the case of materials with a gap Δ , the expression for the permittivity tensor is given by [35]:

$$\begin{aligned} \boldsymbol{\epsilon}(\mathbf{q}) = \mathcal{I} + \frac{\tilde{\mathbf{q}}^2}{\mathbf{q}^2} \frac{e^2 g \boldsymbol{\kappa}^{-1}}{4\pi^2 v_{F,x} v_{F,y} v_{F,z}} & \left[\int_0^1 dx \left\{ x(1-x) \ln \left| \frac{(2\tilde{\Lambda})^2}{\Delta^2 - x(1-x)(\omega^2 - \tilde{\mathbf{q}}^2)} \right| - \frac{5}{18} \right\} \right. \\ & \left. + i \frac{\pi}{6} \sqrt{1 - \frac{4\Delta^2}{\omega^2 - \tilde{\mathbf{q}}^2}} \left(1 + \frac{2\Delta^2}{\omega^2 - \tilde{\mathbf{q}}^2} \right) \Theta(\omega^2 - \tilde{\mathbf{q}}^2 - 4\Delta^2) \right]. \end{aligned} \quad (16)$$

From Eq. (14) and Fig. 1, it is clear that in the scattering limit ($|q^2| \sim \mathbf{q}^2 \gg \omega^2$) the mixing matrix is dominated by the \mathcal{K}_{LL} component. Therefore, for DM scattering there is a negligible mixing between longitudinal and transverse polarizations, and the rate is dominated by the longitudinal degrees of freedom whose in-medium propagator is given by

$$G^{\mu\nu} = \frac{P_L^{\mu\nu}}{q^2(\hat{\mathbf{q}} \cdot \boldsymbol{\epsilon} \cdot \hat{\mathbf{q}})}. \quad (17)$$

Conversely, in the absorption limit, all components of the mixing matrix are of the same order. Hence in-medium propagation gives rise to a sizable mixing. Therefore, to study DM absorption we need to work in the basis defined in Eq. (8) and use the general in-medium propagator given in Eq. (13).

III. PRELIMINARIES: DARK MATTER WIND

The effects we are considering arise because the DM velocity with respect to the detector changes as the Earth rotates around its axis, see Fig. 2. There are two kinds of effects. The

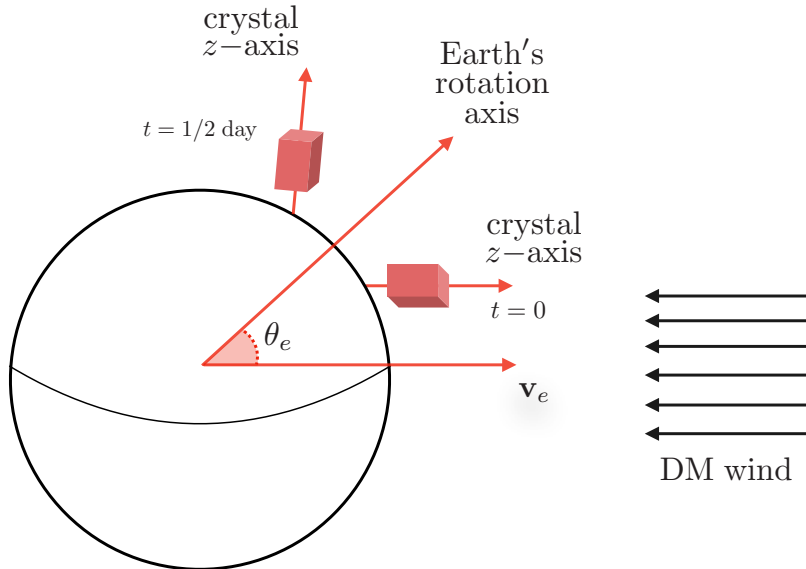


FIG. 2. *Orientation setup of the experimental apparatus.* At $t = 0$ the z -axis of the crystal is aligned with the Earth's velocity (which is approximately in the direction of Cygnus). With this choice for the crystal orientation, the modulation of the signal is independent of the position of the laboratory.

first is kinematic, where the flux of DM particles in the kinematic configuration that can excite a response in the target changes on a daily basis. This effect is dominated by the anisotropy of the Fermi velocity in the material. The second is due to the size of the matrix element, as shown for example in Eq. (17), where the direction of the momentum transfer (typically oriented along the DM wind) changes with respect to the anisotropic permittivity tensor ϵ . We will detail these effects separately for both absorption and scattering below.

But before moving to the results we summarize here our conventions for the DM velocity distribution and the orientation of the DM wind in the crystal rest frame, using a set-up similar to Ref. [39]. For the velocity distribution in the galactic rest frame, $f_{\text{gal}}(\mathbf{v})$, we assume a Maxwellian form, with velocity dispersion $v_0 = 220 \text{ Km/s}$, truncated at $v_{\text{esc}} = 500 \text{ Km/s}$. The velocity distribution in the laboratory frame is related to the one in the galactic frame by $f_{\text{lab}}(\mathbf{v}, t) = f_{\text{gal}}(\mathbf{v} + \mathbf{v}_e(t))$:

$$f_{\text{lab}}(\mathbf{v}, t) = \frac{1}{N_0} \exp \left[-\frac{(\mathbf{v} + \mathbf{v}_e)^2}{v_0^2} \right] \Theta(v_{\text{esc}} - |\mathbf{v} + \mathbf{v}_e|), \quad (18)$$

where $\mathbf{v}_e(t)$ is the Earth's velocity with respect to the DM rest frame due to its revolution around the Sun and N_0 is a normalization constant given by

$$N_0 = \pi^{3/2} v_0^3 \left[\text{erf}\left(\frac{v_{\text{esc}}}{v_0}\right) - \frac{2}{\sqrt{\pi}} \frac{v_{\text{esc}}}{v_0} \exp\left(-\left(\frac{v_{\text{esc}}}{v_0}\right)^2\right) \right]. \quad (19)$$

Parameter	Value for ZrTe ₅ (th.)	Value for ZrTe ₅ (exp.)
(κ_{xx} , κ_{yy} , κ_{zz})	(187.5, 9.8, 90.9)	
($v_{F,x}$, $v_{F,y}$, $v_{F,z}$)	(2.9, 0.5, 2.1) $\times 10^{-3}$	(1.3, 0.65, 1.6) $\times 10^{-3}$
Δ	2.5 meV	11.75 meV
Λ	0.14 keV	
g	4	
V_{uc}	795 Å ³	
ρ_T	6.1 g/cm ³	
n_e	$8.3 \times 10^{23} e^-/\text{kg}$	

TABLE I. *Theoretical and experimental values of the material parameters for ZrTe₅ [35]. Theoretical (experimental) values are used for the curves labeled “th” (“exp”) in plots throughout this paper. For the parameters that were not obtained experimentally, theoretical values are used for both cases.*

The net effect of the Earth’s revolution is to induce a DM wind oriented in the opposite direction of \mathbf{v}_e in the laboratory reference frame. The orientation of \mathbf{v}_e , and therefore of the DM wind, relative to the crystal changes due to the rotation of the Earth. Choosing the crystal orientation such that at $t = 0$ the z-axis in the crystal frame is aligned with the Earth’s velocity the explicit form of \mathbf{v}_e is:

$$\mathbf{v}_e = |\mathbf{v}_e| \begin{pmatrix} \sin \theta_e \sin \phi \\ \sin \theta_e \cos \theta_e (\cos \phi - 1) \\ \cos^2 \theta_e + \sin^2 \theta_e \cos \phi \end{pmatrix} \quad (20)$$

where $|\mathbf{v}_e| \approx 240 \text{ Km/s}$, $\phi = 2\pi \times t/24 \text{ h}$ is the angle parametrizing the rotation of the Earth around its axis and $\theta_e \approx 42^\circ$ is the angle between the Earth’s rotation axis and the direction of its velocity (see Fig. 2 for an illustration of the orientation setup).

IV. ABSORPTION IN ANISOTROPIC DIRAC MATERIALS

The DM absorption rate per unit time and detector mass is given by:

$$R_{abs} = \int d^3\mathbf{v} f_{\text{lab}}(\mathbf{v}, t) R_{abs}(\omega, \mathbf{q}) \quad (21)$$

where $f_{\text{lab}}(\mathbf{v}, t)$ is the DM velocity distribution in the laboratory frame, as defined in the previous section, and $R_{abs}(\omega, \mathbf{q})$ is the DM absorption rate at fixed energy and momentum transfer:

$$R_{abs}(\omega, \mathbf{q}) = \frac{1}{\rho_T} \frac{\rho_\chi}{m_\chi} \langle n_T \sigma_{\text{abs}} v_{\text{rel}} \rangle_{\text{DM}}, \quad (22)$$

where ρ_T is the mass density of the target, n_T the number of target particles, $\sigma_{\text{abs}}(\omega, \mathbf{q})$ the cross section for DM absorption by the target and v_{rel} the relative velocity between the target and the DM. For DM absorption, the energy transfer is uniquely fixed by the DM mass ($\omega = m_\chi$) and the momentum transfer is equal to the DM momentum ($\mathbf{q} = m_\chi \mathbf{v}$).

To derive the absorption rate of dark photons we start by considering the one of ordinary photons. This is related to the optical properties of the medium through the optical theorem:

$$\langle n_T \sigma_{\text{abs}} v_{\text{rel}} \rangle_{\gamma_i} = \frac{1}{\omega} \text{Im} \left[\tilde{\epsilon}_i^\mu \Pi_{\mu\nu} \tilde{\epsilon}_i^\nu \right] = -\frac{1}{\omega} \text{Im} \left[\pi_i(q) \right] \quad (23)$$

where $\tilde{\epsilon}_i$ are the polarization vectors that diagonalize the polarization tensor and $\pi_i(q)$ the corresponding eigenvalues (as discussed in Sec. II). From Eq. (12), we see that the effective mixing between ordinary and dark photons is given by

$$\varepsilon_{\text{eff},i}^2 = \frac{\varepsilon^2 m_{A'}^4}{[m_{A'}^2 - \text{Re} \pi_i(q)]^2 + [\text{Im} \pi_i(q)]^2} \quad (24)$$

and so the dark photon absorption rate at fixed energy and momentum transfer reads

$$R_{\text{abs}}^{A'}(\omega, \mathbf{q}) = -\frac{1}{3} \frac{\rho_\chi}{\rho_T} \sum_{i=1}^3 \varepsilon_{\text{eff},i}^2 \frac{\text{Im} \pi_i(q)}{\omega^2}, \quad (25)$$

where the $1/3$ comes from the average over dark photon polarizations.

In Fig. 3 we show the projected reach for a ZrTe₅ target with a gap of 2.5 meV and 7.5 meV, and we compare it with the one of polar materials [39], superconducting [33] and semiconducting targets [43]. Because of the strong optical response of the superconductor [32, 33] compared to the Dirac Materials, Dirac Materials are far superior in reach for dark photon masses above the band gap: $m_{A'} > 2\Delta$.

The anisotropy of the material induces a dependence of the scattering rate on the orientation of the crystal relative to the DM wind, and this translates to a daily modulation of the absorption signal. The final result, shown in Fig. 4 for the case of ZrTe₅, is that the absorption signal is minimized when the Earth's velocity is aligned with the smallest component of the Fermi velocity of the crystal. We will now explain why it is so.

From Eq. (24) and (25), it is evident that the modulation of the absorption rate is dictated by the \mathbf{q} dependence of the π_i , which (as discussed in section II) are the eigenvalues of the mixing matrix $\mathcal{K}_{AB} = \epsilon_A^\mu \Pi_{\mu\nu} \epsilon_B^\nu$. Specifically, since the denominator of the effective mixing is dominated by the mass term, the absorption rate is dominated by the modulation of $\text{Im} \pi_i$ in the numerator of Eq. (25). Therefore, the rate is minimized when the imaginary part of the π_i is minimized and *vice versa*. The functional form of π_i , for the absorption limit ($\omega \gg |\mathbf{q}|$), can be computed for a specific orientation of \mathbf{q} . This is possible because the mixing matrices,

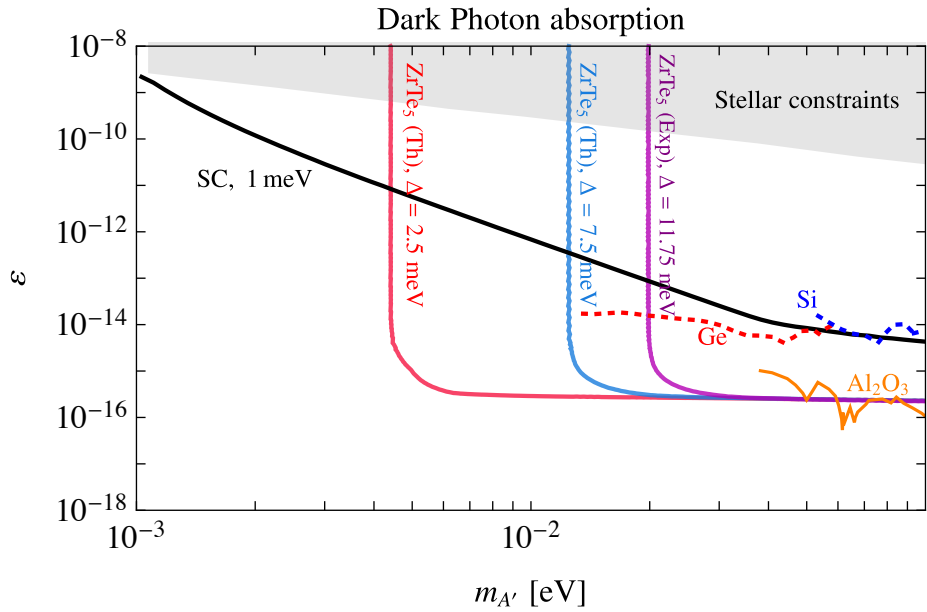


FIG. 3. *Projected reach for the absorption of a kinetically mixed dark photon with a kinetic mixing parameter ε and a mass $m_{A'}$. We show the 95% C.L. sensitivity (3 events) that can be obtained with 1 kg-year exposure of a Dirac material with the (where available, experimental) properties of ZrTe_5 shown in Table I but with a band gap of 2.5 meV (solid red), 7.5 meV (solid blue) and 11.75 meV (solid purple). For comparison we also show the sensitivity of a superconductor with a 1 meV threshold (black line) [33], sapphire (Al_2O_3) with a 1 meV threshold (orange) taken as reference for polar materials [39], and two-phonon excitations in germanium (dotted red) and silicon (dotted blue) semiconductors [43]. The gray shaded region is excluded by stellar emission constraints [44, 45]. The plot is cut at $m_{A'} = 160 \text{ meV}$, which is the largest energy deposit consistent with the linear energy dispersion relation.*

\mathcal{K} and \mathcal{K}' , for two different orientations of the momentum transfer, \mathbf{q} and \mathbf{q}' , are related by a similarity transformation (*i.e.* $\mathcal{K}' = R^T \mathcal{K} R$ where R is a 3-by-3 matrix such that $\mathbf{q}' = R\mathbf{q}$) and therefore have the same eigenvalues. Hence, choosing for example $\mathbf{q} \parallel \hat{z}$, we find that the functional form of the three π_i for the absorption case is given by:

$$\pi_i = \omega^2(1 - \epsilon_{ii}) . \quad (26)$$

From this equation we can now track down the \mathbf{q} dependence of the π_i . This arises from the presence of the $\tilde{\mathbf{q}}^2 \equiv \sum v_{F,i} q_i$ term in the expression of the permittivity tensor, see Eq. (15). Specifically, the $\tilde{\mathbf{q}}^2$ term causes both the imaginary and real part of π_i to be minimized when \mathbf{q} is aligned with the smallest component of the Fermi velocity. Note that the anisotropy of the dielectric tensor κ does not enter the modulation because all components of this tensor receive

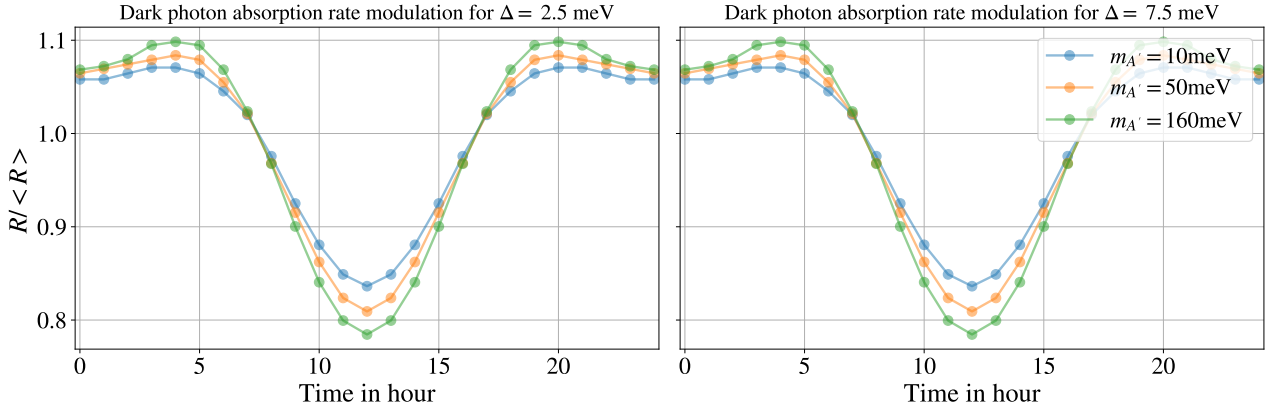


FIG. 4. Left (right) panel shows the modulation of dark photons absorption rate over a sidereal day for the Dirac material ZrTe_5 (using theoretical parameters, see Table I) with a band gap of $\Delta = 2.5$ meV ($\Delta = 7.5$ meV) and for three dark photon masses.

precisely the same modulating factor from $\tilde{\mathbf{q}}$. This explains why for ZrTe_5 the absorption rate is minimized at $t = 1/2$ day, when the DM wind is almost completely in the y -direction; and maximized around $t \approx 1/6$ day and $t \approx 5/6$ day, when the DM wind has the largest component in the x -direction. Thus we conclude that the modulation of the absorption rate is due only to anisotropies of the crystal's band structure (*i.e.* the Fermi velocity), and does not depend on the anisotropy of the dielectric tensor κ .

From Fig. 4 we also see that the amplitude of the modulation decreases as the dark photon mass is lowered. This happens because of the subdominant modulation induced by the effective mixing angle in Eq. (25). By decreasing the dark photon mass, the $\text{Re } \pi_i$ in the denominator of Eq. (24) gives a larger contribution to the effective mixing angle increasing the modulation induced by this term. Therefore, since the modulation induced by the mixing angle (while still being subdominant) is anti-correlated with the one induced by $\text{Im } \pi_i$ in the numerator of Eq. (25), the resulting modulation of the rate is reduced.

V. SCATTERING IN ANISOTROPIC DIRAC MATERIALS

We will characterize the dark matter interaction rate in terms of the target response (the so-called dynamic structure factor $S(q, \omega)$), the dark matter velocity phase space characterized by the DM velocity distribution $f_{\text{gal}}(\vec{v})$, and the nature of the mediator (massless or massive). Then we have the rate to scatter from the valence band of the crystal ($-$, momentum \mathbf{k}) to the

conduction band (+, momentum \mathbf{k}') given by [19]

$$R_{\mathbf{k}, \mathbf{k}'} = \frac{1}{\rho_T m_\chi} \frac{\rho_\chi \pi \bar{\sigma}_e}{\mu_{\chi e}^2} \int \frac{d^3 \mathbf{q}}{(2\pi)^3} \int d^3 \mathbf{v} f_{\text{lab}}(\mathbf{v}) F_{\text{med}}(q)^2 S(\mathbf{q}, \omega), \quad (27)$$

where $\mu_{\chi e}$ is the DM-electron reduced mass,

$$\omega = \frac{1}{2} m_\chi v^2 - \frac{(m_\chi \mathbf{v} - \mathbf{q})^2}{2m_\chi} = \mathbf{q} \cdot \mathbf{v} - \frac{\mathbf{q}^2}{2m_\chi} \quad (28)$$

is the energy deposition, and the dynamic structure factor $S(\mathbf{q}, \omega)$ is

$$S(\mathbf{q}, \omega) = 2\pi \frac{\mathbf{q}^2}{|\mathbf{q} \cdot \epsilon \cdot \mathbf{q}|} \frac{1}{2} \frac{(2\pi)^3}{V} \left(1 - \frac{\tilde{\mathbf{k}} \cdot \tilde{\mathbf{k}}'}{|\tilde{\mathbf{k}}||\tilde{\mathbf{k}}'|} \right) \delta^3(\mathbf{q} - (\mathbf{k}' - \mathbf{k})) \delta(\Delta E_{\mathbf{k}, \mathbf{k}'} - \omega), \quad (29)$$

where V is the volume of the crystal, and the energy splitting from valence to conduction band near the Dirac point is

$$\Delta E_{\mathbf{k}, \mathbf{k}'} = \sqrt{\tilde{\mathbf{k}}^2 + \Delta^2} + \sqrt{\tilde{\mathbf{k}}'^2 + \Delta^2} = \sqrt{\tilde{\mathbf{k}}^2 + \Delta^2} + \sqrt{(\tilde{\mathbf{k}} + \tilde{\mathbf{q}})^2 + \Delta^2}. \quad (30)$$

We utilize a convention where $\bar{\sigma}_e$ is the fiducial cross-section

$$\bar{\sigma}_e = \frac{16\pi \mu_{\chi e}^2 \epsilon^2 \alpha_{\text{EM}} \alpha_D}{q_0^4}, \quad (31)$$

and $F_{\text{med}}(|\mathbf{q}|)$ incorporates the momentum dependence in the scattering cross-section,

$$F_{\text{med}}(|\mathbf{q}|) = q_0^2 / |\mathbf{q}|^2, \quad q_0 = \alpha m_e. \quad (32)$$

Because ω depends on $\mathbf{q} \cdot \mathbf{v}$, the energy conserving delta function can be used to evaluate the velocity integral as proposed in Ref. [39]:

$$\int d^3 v f_{\text{lab}}(\mathbf{v}) \delta(\Delta E - \omega) = \frac{\pi v_0^2}{N_0 |\mathbf{q}|} [\exp(-v_-^2/v_0^2) - \exp(-v_{\text{esc}}^2/v_0^2)] \equiv g(\mathbf{q}, \Delta E_{\mathbf{k}, \mathbf{k}}), \quad (33)$$

where N_0 is a normalization constant defined in Eq. (19), and

$$v_- = \min \left\{ \left| \frac{\mathbf{q} \cdot \mathbf{v}_e + \mathbf{q}^2/2m_\chi + \Delta E}{|\mathbf{q}|} \right|, v_{\text{esc}} \right\} \quad (34)$$

is the minimum velocity (in the galactic reference frame) that a DM particle should have to induce a scattering with energy deposition ΔE and momentum transfer \mathbf{q} . To obtain the total rate, $R_{-, \mathbf{k} \rightarrow +, \mathbf{k}'}$ is summed over initial and final state BZ momenta, over a region of size Λ near Dirac point

$$R_{\text{crystal}} = g_s V^2 \int_{\text{BZ}} \frac{d^3 \mathbf{k} d^3 \mathbf{k}'}{(2\pi)^6} R_{-, \mathbf{k} \rightarrow +, \mathbf{k}'} = g_s g_C V^2 \int_{\text{cone}} \frac{d^3 \mathbf{k} d^3 \mathbf{k}'}{(2\pi)^6} R_{\mathbf{k}, \mathbf{k}'}. \quad (35)$$

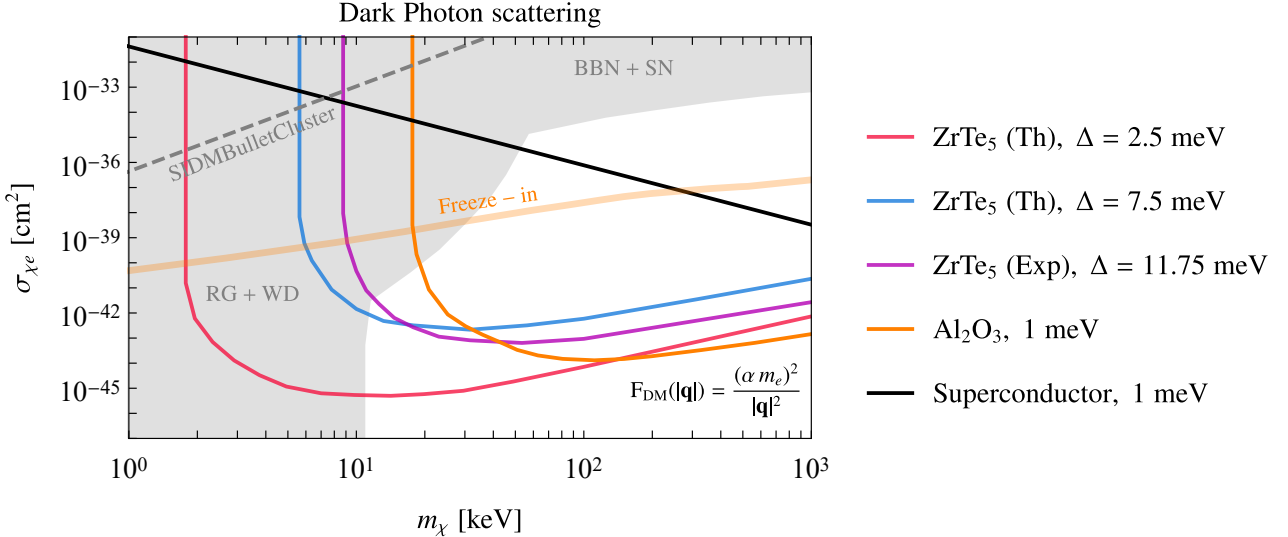


FIG. 5. *Projected reach of dark matter scattering in Dirac material for a background-free 95% C.L. sensitivity (3 events) assuming a 1 kg-year exposure of ZrTe₅ with band gaps of 2.5 meV (red line), 7.5 meV (blue line) and 11.75 meV (purple line). For ZrTe₅ curves, “Th” indicates the use of theoretical parameters, and “Exp” indicates the use of experimental parameters (See Table I). For comparison, we show the respective reaches of superconductors with a 1 meV threshold (black line) [33] and sapphire (Al₂O₃) with a 1 meV threshold (orange line) [38]. The thick orange line indicates the region of parameter space where the freeze-in production results in the correct dark matter relic abundance, as computed in Ref. [15]. Shaded regions are bounds from red giants, white dwarfs, big bang nucleosynthesis and supernovae, and are derived from millicharged particle limits [19, 46]. The dashed line is the self interacting dark matter bound derived from observations of the Bullet Cluster [47].*

The scattering rate per unit time per unit detector mass is then given by

$$R = \frac{\rho_\chi}{m_\chi} \frac{\pi \bar{\sigma}_e}{\mu_{\chi e}^2} \int \frac{d^3 \mathbf{q}}{(2\pi)^3} \int \frac{d^3 \mathbf{k}}{(2\pi)^3} F_{\text{med}}(\mathbf{q})^2 |\langle f | \mathcal{F}_T | i \rangle|^2 g(\mathbf{q}, \Delta E_{\mathbf{k}, \mathbf{k}'}) \quad (36)$$

with

$$|\langle f | \mathcal{F}_T | i \rangle|^2 = \pi g n_e V_{\text{uc}} \underbrace{\frac{\mathbf{q}^2}{|\mathbf{q} \cdot \boldsymbol{\epsilon} \cdot \mathbf{q}|}}_{\epsilon \text{ factor}} \times \underbrace{\left(1 - \frac{\tilde{\mathbf{k}} \cdot (\tilde{\mathbf{k}} + \tilde{\mathbf{q}})}{|\tilde{\mathbf{k}}| |\tilde{\mathbf{k}} + \tilde{\mathbf{q}}|} \right)}_{\text{WF factor}}, \quad (37)$$

where V_{uc} is the volume of the unit cell, n_e is the electron density, and $g = g_s g_C$ is the product of Dirac cone and spin degeneracies. For future convenience, we labeled two factors in the Matrix Element $\sum_f |\langle f | \mathcal{F}_T | i \rangle|^2$ as ϵ and WF factors respectively.

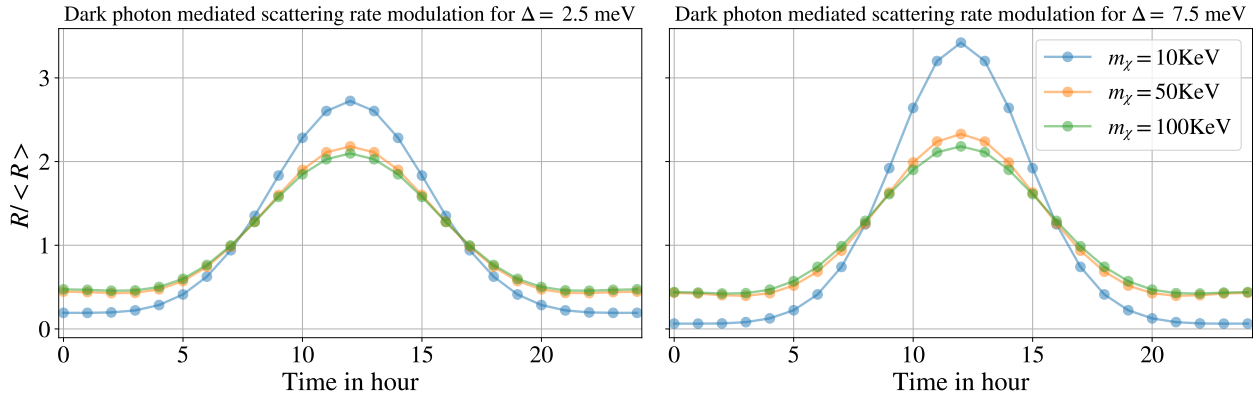


FIG. 6. *Daily modulation of the dark photon mediated scattering rate for ZrTe_5 (using theoretical parameters, see Table I) with a band gap of 2.5 meV (left panel) and 7.5 meV (right panel) for three different dark matter masses.*

In Fig. 5 we show the projected reach for a ZrTe_5 target with gap values of 2.5 meV, 7.5 meV and 11.75 meV, and we compare it with the one of a superconducting target with 1 meV threshold [48]. Because of the strong optical response of the superconductor [32, 33] compared to the Dirac Materials, Dirac Materials are far superior in reach. By contrast, polar materials [38] are competitive with Dirac Materials. Even though sapphire (Al_2O_3) has a better reach at higher masses, the reach of ZrTe_5 with $\Delta = 2.5 \text{ meV}$ is roughly two orders of magnitude better at masses smaller than $\sim 50 \text{ keV}$.

In Fig. 6 we report the daily modulation of the scattering rate for ZrTe_5 for different mass and threshold values. We observe that daily modulation increases for higher masses and thresholds. Also, the rate is maximized around $t = 1/2$ day when the DM wind point along the smallest component of the crystal Fermi velocity. The reason for these behaviors is discussed in detail next.

A. Origin of the daily modulation

The Earth's motion picks out a preferred direction for \mathbf{q} through the minimum velocity, v_- , appearing in the velocity phase space integral Eq. (34). A smaller minimum velocity corresponds to a larger available phase space, and hence a larger $g(\mathbf{q}, \Delta E_{\mathbf{k}, \mathbf{k}'})$ and a larger rate. As shown in Fig. 7, this function is maximized when \mathbf{q} is antiparallel to \mathbf{v}_e .

This correlation of \mathbf{q} with the Earth's velocity feeds through to crystal anisotropies in two ways. First, it appears through the anisotropy in the Fermi velocity; the kinematics prefers

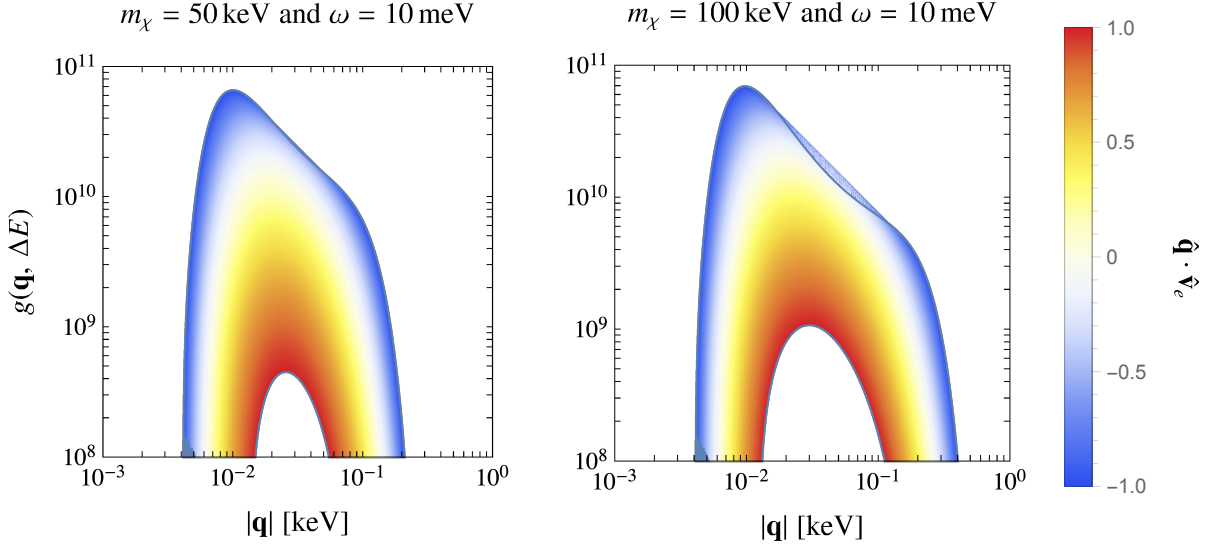


FIG. 7. Value of the kinematic factor $g(\mathbf{q}, \Delta E)$ for different orientations of \mathbf{q} with respect to \mathbf{v}_e , specifically the value of the dot product $\hat{\mathbf{q}} \cdot \hat{\mathbf{v}}_e$ is indicated by the color map.

that the Earth's motion be anti-aligned with the direction of the smallest Fermi velocity, in order to increase the available phase space. We refer to this as a kinematic effect. And second it affects the magnitude of the scattering matrix element, $|\langle f | \mathcal{F}_T | i \rangle|$, through the so-called ϵ and “WF” factors labeled in Eq. (37). We now discuss the preferred direction singled out by each one of these two elements, and which effect plays the most important role in the case of ZrTe₅.

1. Anisotropies in Kinematics

The kinematics of the scattering is sensitive to anisotropies in the Fermi velocity due to the rescaled momentum $\tilde{\mathbf{k}}$ and $\tilde{\mathbf{q}}$ that appear in $\Delta E_{\mathbf{k}, \mathbf{k}'}$. From Eq. (30) we can see that, for a given \mathbf{k} , the energy transfer is minimized when \mathbf{q} is aligned with the smallest component of the Fermi velocity. Therefore, when \mathbf{q} points in this direction, a larger fraction of momenta in the BZ is kinematically allowed, so that the rate is maximized. This is shown in Fig. 8, where the rate is maximized when the DM wind, and hence \mathbf{q} , is in the direction of the smallest component of the Fermi velocity.

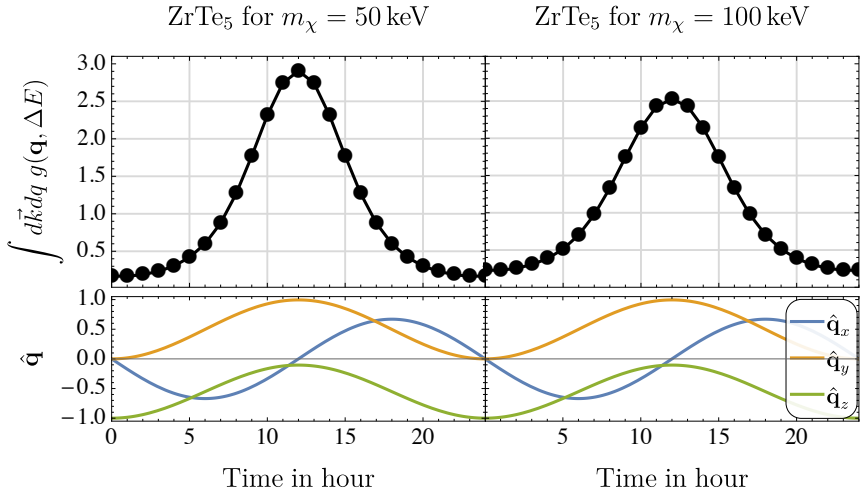


FIG. 8. *Modulation of the kinematic factor over a sidereal day.* The reported values (which are normalized to the daily average) are obtained by integrating over the magnitude of \mathbf{q} while keeping its orientation anti-aligned with the Earth's velocity: $\hat{\mathbf{q}} = -\mathbf{v}_e(t)$. We see that the kinematic factor is maximized when \mathbf{q} points along the y -direction, which corresponds to the smallest component of v_F for ZrTe₅.

2. Anisotropies in the Matrix Element

The scattering matrix element is sensitive to anisotropies in both the band structure and the permittivity tensor. To understand the modulation induced by the matrix element it is useful to deconstruct the impact on the matrix element in terms of the ϵ and WF factors defined in Eq. (37).

Crystal anisotropies enter in the ϵ -factor in two ways. First, the presence of the κ^{-1} matrix in Eq. (15) is such that the ϵ -factor is larger when \mathbf{q} points in the direction of the largest component of the dielectric tensor. Second, the $\tilde{\mathbf{q}}^2 \equiv \sum v_{F,i} q_i$ in Eq. (15) causes the ϵ -factor to be maximized when \mathbf{q} is aligned with the smallest component of the Fermi velocity and vice-versa. In general, one can convince oneself from the Kramers-Kronig sum rules, that the direction corresponding to the largest component of the dielectric tensor corresponds to the one with a small gap and hence the smallest Fermi velocity. Therefore, the resulting modulation of the ϵ -term tends to present more than one local minimum/maxima. The dependence of the ϵ -factor on the \mathbf{q} -orientation relative to the crystal anisotropies is illustrated in Fig. 9 for the case of ZrTe₅.

The WF-factor is sensitive to anisotropies in the band structure of the crystal through the

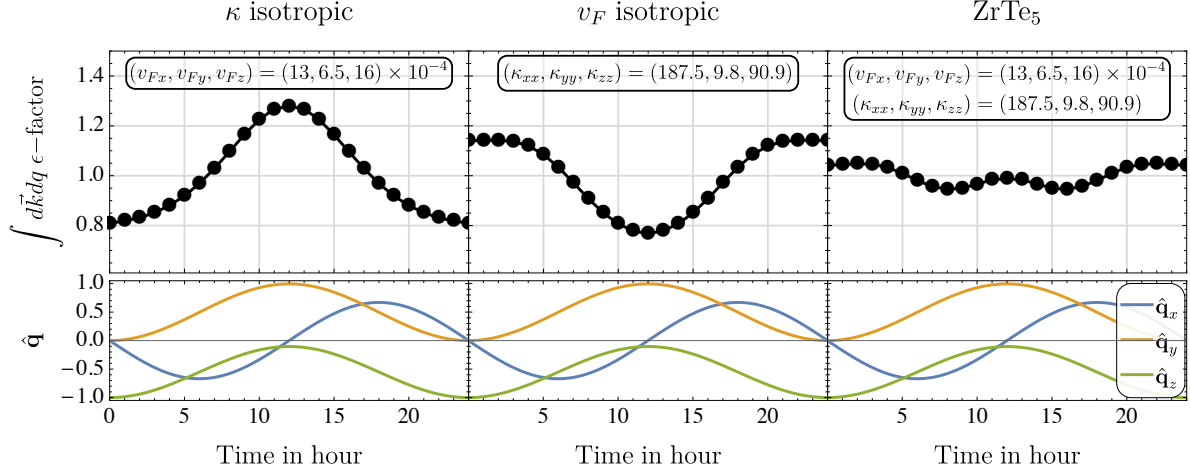


FIG. 9. Modulation of the ϵ -factor (using theoretical parameters, see Table I) over a sidereal day for $\hat{\mathbf{q}} = -\mathbf{v}_e(t)$. To disentangle the modulation induced by anisotropies in the permittivity tensor from the one induced by the Fermi velocity, we show in the first (second) panel the modulation (normalized to the daily average) for a hypothetical crystal with isotropic κ (v_F). While the realistic case of ZrTe₅ is shown in the third panel. As discussed in the text, anisotropies in the band structure prefer momentum transfers aligned with the smallest component of v_F , while the dielectric tensor picks out a momentum transfer aligned in the direction of largest κ . For ZrTe₅, these two directions are orthogonal and this translates in a suppressed daily modulation of the ϵ -factor, as can be seen in the third panel.

rescaled momentum transfer $\tilde{\mathbf{q}}$. The WF-factor grows by increasing the angle between $\tilde{\mathbf{q}}$ and $\tilde{\mathbf{q}} + \tilde{\mathbf{k}}$. This angle is non-zero when $\tilde{\mathbf{q}}$ gives a sizable contribution to the sum $\tilde{\mathbf{q}} + \tilde{\mathbf{k}}$. The fraction of the kinematically allowed \mathbf{q} that satisfies this requirement grows when the momentum transfer is aligned with the largest component of the Fermi velocity, given that this maximized the rescaled momenta $\tilde{\mathbf{q}}$. The WF-factor is maximized (minimized) when the momentum transfer points along the direction with the highest (smallest) Fermi velocity, as shown in Fig. 10.

Comparing figures 8, 9 and 10, we see that for the case of ZrTe₅ the modulation of the rate is dominated by the kinematic term. This explains why the scattering rate shown in Fig. 6 is maximized around $t = 1/2$ day. Indeed, at this time the Earth's velocity is almost completely in the y -direction. Therefore, the preferred direction for \mathbf{q} singled out by the Earth's motion ($\hat{\mathbf{q}} = -\mathbf{v}_e$) and the one singled out by the kinematic term ($\hat{\mathbf{q}}$ along the smallest component of v_F) are aligned.

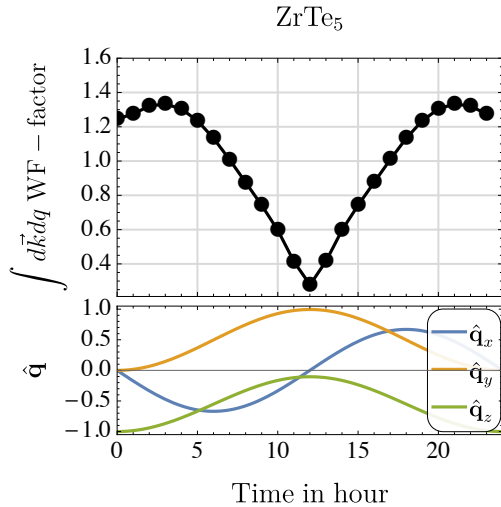


FIG. 10. *Modulation of the WF-factor (using theoretical parameters, see Table I) (normalized to the daily average) over a sidereal day for $\hat{\mathbf{q}} = -\mathbf{v}_e(t)$. As discussed in the text, the WF-term is minimized when \mathbf{q} points along the direction corresponding to the smallest component of the Fermi velocity.*

VI. CONCLUSIONS

Dirac materials, due to their peculiar band structure near the Fermi surface that prevents the photon from developing an in-medium effective mass, are promising targets to look for dark photon-mediated scatterings and absorption of light dark matter. In this work we discussed how anisotropies in both the Fermi velocities and the permittivity tensor give rise to a daily modulation of the DM interaction rate with a Dirac material.

To this end, we generalized the discussion of Ref. [35] to accurately take into account anisotropies of the crystal structure, which induce a mixing of the longitudinal and transverse dark photon polarizations during their propagation in the media. We then applied these results to the specific case of the Dirac material $ZrTe_5$, giving a more precise determination of the projected reach (see Fig. 3 and Fig. 5) and finding a daily modulation of $\mathcal{O}(1)$ (see Fig. 4 and Fig. 6) for both scattering and absorption signals.

Since the shape of the modulation signal depends on the orientation of the crystal with respect to the dark matter wind, these modulation effects can be used to validate any putative dark matter signal simply by changing the orientation of the crystal and observing a change in the shape of the modulation. Moreover, since the amplitude of the modulation (both for absorption and scattering signals) depends on the DM mass, a definitive observation of the modulation could be used to infer the value of the DM mass.

ACKNOWLEDGMENTS

We thank Tanner Trickle and Kevin Zhang for discussions, and Yoni Kahn for comments on the draft. This work was supported by the Quantum Information Science Enabled Discovery (QuantISED) for High Energy Physics (KA2401032) at LBNL.

Appendix A: In medium polarization tensor

In this appendix we relate the in-medium vacuum polarization tensor to the optical response of the medium. To do this we will use the two following relations [49]:²

$$J_\mu = -\Pi_{\mu\nu}A^\nu \quad (\text{A1})$$

$$J^i = \sigma_j^i E^j \quad (\text{A2})$$

where σ_{ij} is the conductivity tensor.

- Π_{ij}, Π_{0i} : using eq.(A2) and taking the spatial component of eq.(A1) we get:

$$\begin{cases} J_i = -\Pi_{ij}A^j - \Pi_{i0}A^0 \\ J_i = \sigma_{ij}E^j = \sigma_{ij}(i\omega A^j - iq^j A_0) \end{cases} \quad (\text{A3})$$

where in the second equation we have used the Maxwell equation $E^j = i\omega A^j - iq^j A_0$. From this we see that

$$\Pi_{ij} = -i\omega\sigma_{ij} \quad (\text{A4})$$

$$\Pi_{i0} = i\sigma_{ij}q^j \quad (\text{A5})$$

- Π_{00} : For the 00 component things are more complicated. In the non-relativistic (NR) limit we can infer Π_{00} from the Coulomb potential generated by a point-like charge, since they are related by $G_{00} = -V(q)/e^2$. The form of the Columb potential in a anisotropic dielectric medium is given by [50]:

$$V(\vec{q}) = \frac{e^2}{\vec{q} \cdot \epsilon \cdot \vec{q}} \quad (\text{A6})$$

² To be precise the relation between J and Π is given by $J_\mu = -R_{\mu\nu}A^\nu$ and the imaginary part of R and Π have a different sign when ω is negative. This does not seems to be ever important for us.

where the permittivity tensor, ϵ , is related to the conductivity tensor by $\sigma = i\omega(1 - \epsilon)$. From this follows that the 00 component of the in-medium propagator, in the NR limit, is given by:

$$G_{00}\Big|_{\text{NR}} = -\frac{1}{\vec{q} \cdot \epsilon \cdot \vec{q}} \implies \Pi_{00}\Big|_{\text{NR}} = -|\vec{q}|^2(1 - \hat{q} \cdot \epsilon \cdot \hat{q}). \quad (\text{A7})$$

To derive the expression of Π_{00} in the relativistic regime, we start from Eq. (A2) which, together with current conservation $\partial_\mu J^\mu = 0$ and Maxwell equation $E^j = i\omega A^j - iq^j A_0$, gives:

$$\omega J_0 = iq^i \sigma_{ij} (\omega A^j - q^j A^0). \quad (\text{A8})$$

Therefore, using that $\Pi_{0i} = i\sigma_{ij}q^j$ and that in Coulomb gauge $\Pi_{0i}A^i = 0$ we get

$$\Pi_{00} = \frac{i}{\omega} \vec{q} \cdot \sigma \cdot \vec{q} \quad (\text{A9})$$

which in the NR limit reduces to eq.(A7).

- [1] M. J. Strassler and K. M. Zurek, *Echoes of a hidden valley at hadron colliders*, *Phys. Lett.* **B651** (2007) 374–379, [[hep-ph/0604261](#)].
- [2] C. Boehm and P. Fayet, *Scalar dark matter candidates*, *Nucl. Phys.* **B683** (2004) 219–263, [[hep-ph/0305261](#)].
- [3] M. Pospelov, A. Ritz and M. B. Voloshin, *Secluded WIMP Dark Matter*, *Phys. Lett.* **B662** (2008) 53–61, [[0711.4866](#)].
- [4] D. Hooper and K. M. Zurek, *A Natural Supersymmetric Model with MeV Dark Matter*, *Phys. Rev.* **D77** (2008) 087302, [[0801.3686](#)].
- [5] J. Kumar and J. L. Feng, *WIMPless Dark Matter*, *AIP Conf. Proc.* **1200** (2010) 1059–1062, [[0909.2877](#)].
- [6] D. E. Kaplan, M. A. Luty and K. M. Zurek, *Asymmetric Dark Matter*, *Phys. Rev.* **D79** (2009) 115016, [[0901.4117](#)].
- [7] T. Cohen, D. J. Phalen, A. Pierce and K. M. Zurek, *Asymmetric Dark Matter from a GeV Hidden Sector*, *Phys. Rev.* **D82** (2010) 056001, [[1005.1655](#)].
- [8] N. Arkani-Hamed and N. Weiner, *LHC Signals for a SuperUnified Theory of Dark Matter*, *JHEP* **12** (2008) 104, [[0810.0714](#)].
- [9] C. Cheung, J. T. Ruderman, L.-T. Wang and I. Yavin, *Kinetic Mixing as the Origin of Light Dark Scales*, *Phys. Rev.* **D80** (2009) 035008, [[0902.3246](#)].

- [10] D. E. Morrissey, D. Poland and K. M. Zurek, *Abelian Hidden Sectors at a GeV*, *JHEP* **07** (2009) 050, [[0904.2567](#)].
- [11] L. J. Hall, K. Jedamzik, J. March-Russell and S. M. West, *Freeze-In Production of FIMP Dark Matter*, *JHEP* **03** (2010) 080, [[0911.1120](#)].
- [12] Y. Hochberg, E. Kuflik, T. Volansky and J. G. Wacker, *Mechanism for Thermal Relic Dark Matter of Strongly Interacting Massive Particles*, *Phys. Rev. Lett.* **113** (2014) 171301, [[1402.5143](#)].
- [13] T. Lin, H.-B. Yu and K. M. Zurek, *On Symmetric and Asymmetric Light Dark Matter*, *Phys. Rev.* **D85** (2012) 063503, [[1111.0293](#)].
- [14] X. Chu, T. Hambye and M. H. G. Tytgat, *The Four Basic Ways of Creating Dark Matter Through a Portal*, *JCAP* **1205** (2012) 034, [[1112.0493](#)].
- [15] C. Dvorkin, T. Lin and K. Schutz, *Making dark matter out of light: freeze-in from plasma effects*, *Phys. Rev.* **D99** (2019) 115009, [[1902.08623](#)].
- [16] M. Battaglieri et al., *US Cosmic Visions: New Ideas in Dark Matter 2017: Community Report*, in *U.S. Cosmic Visions: New Ideas in Dark Matter College Park, MD, USA, March 23-25, 2017*, 2017, [1707.04591](#), <http://lss.fnal.gov/archive/2017/conf/fermilab-conf-17-282-ae-ppd-t.pdf>.
- [17] R. Essig, J. Mardon and T. Volansky, *Direct Detection of Sub-GeV Dark Matter*, *Phys. Rev.* **D85** (2012) 076007, [[1108.5383](#)].
- [18] P. W. Graham, D. E. Kaplan, S. Rajendran and M. T. Walters, *Semiconductor Probes of Light Dark Matter*, *Phys. Dark Univ.* **1** (2012) 32–49, [[1203.2531](#)].
- [19] R. Essig, M. Fernandez-Serra, J. Mardon, A. Soto, T. Volansky and T.-T. Yu, *Direct Detection of sub-GeV Dark Matter with Semiconductor Targets*, *JHEP* **05** (2016) 046, [[1509.01598](#)].
- [20] R. Essig, A. Manalaysay, J. Mardon, P. Sorensen and T. Volansky, *First Direct Detection Limits on sub-GeV Dark Matter from XENON10*, *Phys. Rev. Lett.* **109** (2012) 021301, [[1206.2644](#)].
- [21] R. Essig, T. Volansky and T.-T. Yu, *New Constraints and Prospects for sub-GeV Dark Matter Scattering off Electrons in Xenon*, *Phys. Rev.* **D96** (2017) 043017, [[1703.00910](#)].
- [22] SENSEI collaboration, M. Crisler, R. Essig, J. Estrada, G. Fernandez, J. Tiffenberg, M. Sofo haro et al., *SENSEI: First Direct-Detection Constraints on sub-GeV Dark Matter from a Surface Run*, *Phys. Rev. Lett.* **121** (2018) 061803, [[1804.00088](#)].
- [23] SENSEI collaboration, J. Tiffenberg, M. Sofo-Haro, A. Drlica-Wagner, R. Essig, Y. Guardincerri, S. Holland et al., *Single-electron and single-photon sensitivity with a silicon Skipper CCD*, *Phys. Rev. Lett.* **119** (2017) 131802, [[1706.00028](#)].
- [24] SENSEI collaboration, O. Abramoff et al., *SENSEI: Direct-Detection Constraints on Sub-GeV Dark Matter from a Shallow Underground Run Using a Prototype Skipper-CCD*, *Phys. Rev. Lett.*

- 122** (2019) 161801, [[1901.10478](#)].
- [25] DAMIC collaboration, A. Aguilar-Arevalo et al., *Search for low-mass WIMPs in a 0.6 kg day exposure of the DAMIC experiment at SNOLAB*, *Phys. Rev.* **D94** (2016) 082006, [[1607.07410](#)].
- [26] DAMIC collaboration, A. Aguilar-Arevalo et al., *Constraints on Light Dark Matter Particles Interacting with Electrons from DAMIC at SNOLAB*, [1907.12628](#).
- [27] SUPERCDMS collaboration, R. Agnese et al., *Search for Low-Mass Weakly Interacting Massive Particles with SuperCDMS*, *Phys. Rev. Lett.* **112** (2014) 241302, [[1402.7137](#)].
- [28] SUPERCDMS collaboration, R. Agnese et al., *New Results from the Search for Low-Mass Weakly Interacting Massive Particles with the CDMS Low Ionization Threshold Experiment*, *Phys. Rev. Lett.* **116** (2016) 071301, [[1509.02448](#)].
- [29] R. K. Romani et al., *Thermal detection of single e-h pairs in a biased silicon crystal detector*, *Appl. Phys. Lett.* **112** (2018) 043501, [[1710.09335](#)].
- [30] SUPERCDMS collaboration, R. Agnese et al., *First Dark Matter Constraints from a SuperCDMS Single-Charge Sensitive Detector*, *Phys. Rev. Lett.* **121** (2018) 051301, [[1804.10697](#)].
- [31] SUPERCDMS collaboration, R. Agnese et al., *Search for Low-Mass Dark Matter with CDMSlite Using a Profile Likelihood Fit*, *Phys. Rev.* **D99** (2019) 062001, [[1808.09098](#)].
- [32] Y. Hochberg, Y. Zhao and K. M. Zurek, *Superconducting Detectors for Superlight Dark Matter*, *Phys. Rev. Lett.* **116** (2016) 011301, [[1504.07237](#)].
- [33] Y. Hochberg, M. Pyle, Y. Zhao and K. M. Zurek, *Detecting Superlight Dark Matter with Fermi-Degenerate Materials*, *JHEP* **08** (2016) 057, [[1512.04533](#)].
- [34] Y. Hochberg, Y. Kahn, M. Lisanti, C. G. Tully and K. M. Zurek, *Directional detection of dark matter with two-dimensional targets*, *Phys. Lett.* **B772** (2017) 239–246, [[1606.08849](#)].
- [35] Y. Hochberg, Y. Kahn, M. Lisanti, K. M. Zurek, A. G. Grushin, R. Ilan et al., *Detection of sub-MeV Dark Matter with Three-Dimensional Dirac Materials*, *Phys. Rev.* **D97** (2018) 015004, [[1708.08929](#)].
- [36] S. Knapen, T. Lin and K. M. Zurek, *Light Dark Matter in Superfluid Helium: Detection with Multi-excitation Production*, *Phys. Rev.* **D95** (2017) 056019, [[1611.06228](#)].
- [37] K. Schutz and K. M. Zurek, *Detectability of Light Dark Matter with Superfluid Helium*, *Phys. Rev. Lett.* **117** (2016) 121302, [[1604.08206](#)].
- [38] S. Knapen, T. Lin, M. Pyle and K. M. Zurek, *Detection of Light Dark Matter With Optical Phonons in Polar Materials*, *Phys. Lett.* **B785** (2018) 386–390, [[1712.06598](#)].
- [39] S. Griffin, S. Knapen, T. Lin and K. M. Zurek, *Directional Detection of Light Dark Matter with Polar Materials*, *Phys. Rev.* **D98** (2018) 115034, [[1807.10291](#)].
- [40] R. Budnik, O. Chesnovsky, O. Slone and T. Volansky, *Direct Detection of Light Dark Matter*

and Solar Neutrinos via Color Center Production in Crystals, *Phys. Lett.* **B782** (2018) 242–250, [[1705.03016](#)].

- [41] S. Rajendran, N. Zobrist, A. O. Sushkov, R. Walsworth and M. Lukin, *A method for directional detection of dark matter using spectroscopy of crystal defects*, *Phys. Rev.* **D96** (2017) 035009, [[1705.09760](#)].
- [42] F. Kadribasic, N. Mirabolfathi, K. Nordlund, A. E. Sand, E. Holmström and F. Djurabekova, *Directional sensitivity in light-mass dark matter searches with single-electron-resolution ionization detectors*, *Phys. Rev. Lett.* **120** (Mar, 2018) 111301.
- [43] Y. Hochberg, T. Lin and K. M. Zurek, *Absorption of light dark matter in semiconductors*, *Phys. Rev.* **D95** (2017) 023013, [[1608.01994](#)].
- [44] H. An, M. Pospelov, J. Pradler and A. Ritz, *Direct Detection Constraints on Dark Photon Dark Matter*, *Phys. Lett.* **B747** (2015) 331–338, [[1412.8378](#)].
- [45] H. An, M. Pospelov and J. Pradler, *Dark Matter Detectors as Dark Photon Helioscopes*, *Phys. Rev. Lett.* **111** (2013) 041302, [[1304.3461](#)].
- [46] S. Davidson, S. Hannestad and G. Raffelt, *Updated bounds on millicharged particles*, *JHEP* **05** (2000) 003, [[hep-ph/0001179](#)].
- [47] J. L. Feng, M. Kaplinghat and H.-B. Yu, *Halo Shape and Relic Density Exclusions of Sommerfeld-Enhanced Dark Matter Explanations of Cosmic Ray Excesses*, *Phys. Rev. Lett.* **104** (2010) 151301, [[0911.0422](#)].
- [48] Y. Hochberg, T. Lin and K. M. Zurek, *Detecting Ultralight Bosonic Dark Matter via Absorption in Superconductors*, *Phys. Rev.* **D94** (2016) 015019, [[1604.06800](#)].
- [49] Schrieffer, *Theory of Superconductivity*, Westview Press.
- [50] C. Verdi and F. Giustino, *Fröhlich electron-phonon vertex from first principles*, *Phys. Rev. Lett.* **115** (Oct, 2015) 176401.